In Situ Measurements of Potential, Current and Charging Current across an EDL Capacitance Anode for an Aqueous Sodium Hybrid Battery

Katherine C. Hess, Jay F. Whitacre and Shawn Litster

J. Electrochem. Soc. 2012, Volume 159, Issue 8, Pages A1351-A1359.
doi: 10.1149/2.028208jes

Journal of The Electrochemical Society, **159** (8) A1351-A1359 (2012)
0013-4651/2012/159(8)/A1351/9/$28.00 © The Electrochemical Society

In Situ Measurements of Potential, Current and Charging Current across an EDL Capacitance Anode for an Aqueous Sodium Hybrid Battery

Katherine C. Hess,[a,*] Jay F. Whitacre,[b,c] and Shawn Litster[a,z]

[a]*Department of Mechanical Engineering, Carnegie Mellon University, Pittsburgh, Pennsylvania 15213, USA*
[b]*Department of Materials Science and Engineering, Carnegie Mellon University, Pittsburgh, Pennsylvania 15213, USA*
[c]*Department of Engineering and Public Policy, Carnegie Mellon University, Pittsburgh, Pennsylvania 15213, USA*

This paper presents a novel method for obtaining in situ, through-thickness measurements of potential, current, charging current, and charge stored or discharged across capacitor and battery electrodes. Here we apply the method to an electrochemical double layer capacitance (EDLC) negative electrode for an aqueous sodium hybrid battery. In this approach, an electrode scaffold (ES) is used to directly measure the electric potential at discrete distances through the electrode under charging and discharging conditions. Finite difference methods are used to calculated local current and charging/discharging rates. The distributions obtained from these measurements are used to show non-uniform charging across an ultra-thick electrode intended for high area-specific energy storage in grid-scale energy storage applications. Using the ES we are able to gain insight into several complex phenomena that cannot be directly observed by other methods. For instance, we identify the portions of the electrode that are underutilized as well as the location of stray, parasitic currents.
 [DOI: 10.1149/2.028208jes]

Manuscript submitted April 5, 2012; revised manuscript received May 9, 2012. Published July 20, 2012. This was Paper 1635 presented at the Montreal, QC, Canada, Meeting of the Society, May 1-6, 2011.

Advanced energy storage technologies are crucial for the integration of renewable electricity into the grid and for improving grid reliability. They are also needed to allow for more effective peak-shaving/load-shifting strategies, as well as to provide a more efficient means for operating long duration ancillary services.[1–3] Energy storage technologies for grid-scale storage must be efficient, reliable, environmentally benign, versatile and cost effective, with capital cost likely to be one key factor in widespread commercialization.[3–5] While there are many technologies being developed for grid-scale energy storage, such as flywheels, flow batteries and pumped hydro, this study is an assessment of a relatively new technology: aqueous electrolyte asymmetric hybrid supercapacitors that use sodium as the functional cation.[6,7]

Asymmetric and/or hybrid batteries combine an intercalation electrode, commonly used in Li-ion batteries, with an electrochemical double layer capacitance (EDLC) electrode, typically found in supercapacitors. Aqueous sodium hybrid devices in particular, feature a Na-ion based positive intercalation electrode and use an aqueous electrolyte. In this study we have chosen to focus on an aqueous sodium hybrid battery reported by Whitacre et al.,[8] which uses $Na_4Mn_9O_{18}$ for the intercalation positive electrode and activated carbon for the negative electrode in combination with Na_2SO_4 as the aqueous sodium electrolyte. During charging, Na^+ ions de-intercalate from the $Na_4Mn_9O_{18}$ positive electrode crystal structure and diffuse toward the negative electrode. In the negative electrode, Na^+ ions diffuse through the electrolyte-filled pores in the activated carbon and store charge by electrostatically adsorbing at the negatively charged carbon surface. It is in the negative electrode where most of the losses associated with ionic transport occur and the most improvements must be made.

Specifically, the losses in the negative electrode are due to the finite mobilities of the ions and the limited transport rates across the electrode thickness. This issue is exacerbated in the negative electrode by the fact that the accessible charge-storage capacities of the positive and negative electrodes must be properly balanced leading to a relatively thick negative electrode as compared to the positive electrode because of its lower volumetric energy density.[6] Furthermore, one way to improve the commercial viability of these and Li-ion batteries is to increase the electrode thicknesses so that more charge can be stored with less geometric area (i.e., separator area and current collector). If adequate power density is maintained, thicker electrodes lead to lower costs for non-functional materials, such as the separator, current collectors and packaging.[9,10] A key advantage of aqueous electrolytes over organic electrolytes, besides being inflammable, is the higher ion mobilities. The mobility of sodium ions in water is 10^4 times that for lithium ions in a typical Li-ion battery organic electrolyte.[11,12] This higher mobility also means the aqueous transport times-scales are 100 times higher, enabling thicker electrodes. For example, Li-ion battery electrodes are typically less than 100 μm thick due to Li^+ transport limitations in organic electrolytes, even though dramatic and necessary cost reductions could be achieved if thicker electrodes with adequate power density were possible.[13] For this reason, we focus here on the negative electrode|electrolyte system for this aqueous hybrid battery, operating it in a symmetric EDLC for simplified implementation.

Figure 1 shows a cross-section schematic of the symmetric EDLC used in this study during charging. Charging occurs when a positive voltage is applied to the cell's positive electrode and electrons begin to travel away from the positive electrode toward the negative electrode. A positive surface charge forms on the activated carbon in the positive electrode, while a negative surface charge forms on the activated carbon in the negative electrode. These surface charges in the electron conducting phase are locally shielded by sulfate and sodium ions from the electrolyte, respectively, forming EDLs. Transmission-line models of EDLCs show multiple resistances in parallel through the thickness of the electrode, representing impedances in the carbon structure and electrolyte that hinder the transport of ions through the electrode.[14] This suggests that charging will begin quickly with ions filling unoccupied sites in the material near the separator, but will slow dramatically over time, leading to difficulties in fully utilizing the electrode. Further characterization of the EDLC electrode must be conducted to study and improve transport rates, and thereby the performance, of thick electrodes. This will lead to lower costs of non-functional materials, making the EDLC electrodes more economically viable in grid-scale energy storage technology.

A number of studies have previously been conducted to measure distributions and gather a more comprehensive understanding of electrode charging and discharging cycles. Liu et al.[15] used synchrotron X-ray microdiffraction to obtain state-of-charge profiles, both in-plane and through-plane, in a $LiFePO_4$ battery electrodes. However, they had to "freeze" the charge distribution by breaking the load circuit and conduct the X-ray microdiffraction post-mortem, preventing transient measurements during discharging and charging. Their work required a large number of repeated, complex experiments for analyzing any

*Electrochemical Society Student Member.
zE-mail: Litster@andrew.cmu.edu

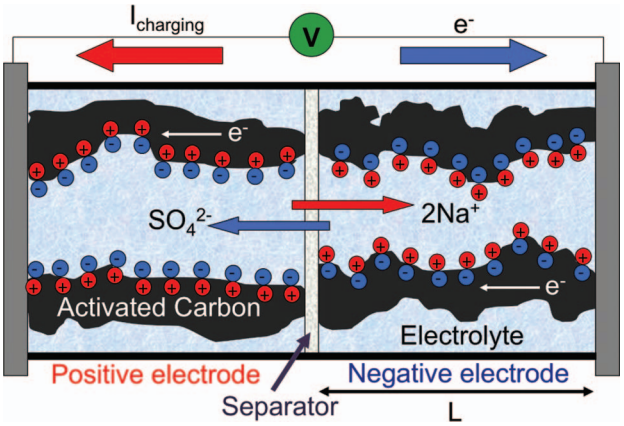

Figure 1. This figure depicts the cross-section of a symmetric EDLC cell during charging. A positive voltage is applied to the positive electrode, and drives sodium and sulfate ions from the electrolyte toward the negative and positive electrodes respectively.

transient effects or parametric studies with statistical confidence. Harris et al.[12] used the color changing properties of graphite to visualize the insertion of lithium into the electrode as it charged. While this method enables transient visualizations, it is only semi-quantitative and is restricted to the Li-ion|graphite electrode system. Ng et al.[16] developed a quantitative, multiple working electrode (MWE) method for measuring charging distributions. The MWEs, which each had their own mesh current collector and were electrically isolated from one another using additional separators, were stacked on top of each other and used to obtain current density measurements at three points through the thickness of a Li-ion negative electrode. While they were the first to gather these types of distributions through a battery electrode, the separators and current collectors intrude significantly upon the normal electrode structure, and make it unrepresentative of those used in a typical Li-ion battery. In addition, the macroscale current collectors and separators limit the resolution of this approach. A recent study by Siegel et al.[17] used neutron imaging to look at the change in Li concentrations through a $LiFePO_4$ battery electrode during charging and discharging. They were able to visualize the changes in Li concentration, but there were a number of sources of uncertainty in their measurements, such as possible improper alignment and surface roughness. Additionally, as Siegel et al. discuss, radiography imaging requires trade-offs between spatial measurement accuracy and temporal resolution. Finally, all of these studies have been conducted on Li-ion battery electrodes whereas we are interested in studying distributions in aqueous Na batteries and EDLCs. Of the above methods, only the multiple working electrode approach of Ng et al. is viable for these batteries, but it is intrusive and offers a limited number of measurements.

We have recently developed a new technique for measuring in situ distributions through electrodes using an electrode scaffold (ES). We previously used this approach to measure electrolyte potential distributions through a polymer electrolyte fuel cell (PEFC) cathode with 8.5 μm resolution.[18] To the best of our knowledge, the ES analysis presented here is the first set of quantitative, in situ distribution measurements of current, charging current, and charge stored in a continuous battery or EDLC electrode. The ES, as Figure 2 shows, is made up of alternating insulating and sensing layers that surround a column of electrode material. Depending on the sensing material and instrumentation, the ES can provide measurements of various physicochemical properties, including electric potential, ionic potential,[18] and species sensing.[19] As reported here, the multiple, through-thickness sensing layers enable the measurement of local conductivities, as well as potentials, which lead to quantitative estimations of currents, charging currents, and charge stored through numerical methods. A key benefit of the ES approach is that it does not alter the electrode structure or intrude on the normal, macro-scale one-dimensional transport. However, the electrode must be structured as a high aspect ratio cylinder to ensure 1-D transport, which is required for accurate measurements from the sensing layers.

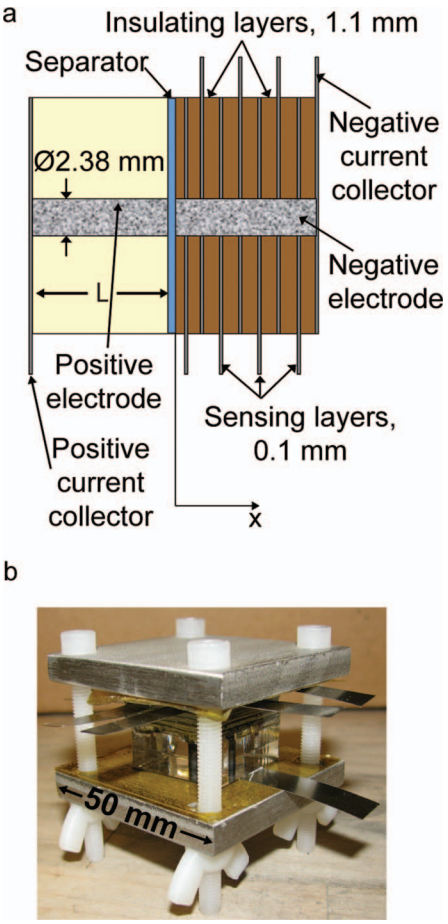

Figure 2. a. Schematic of the ES cross-section showing the alternating sensing and insulating layers on the negative electrode. b. A photo of an assembled ES.

In this paper, we use an ES for measuring the through-thickness electric potential distribution in the negative electrode of a thick, symmetric, aqueous Na EDLC such as those used in hybrid batteries for grid-scale energy storage. The potentials were measured during both potentiostatic charging and galvanostatic discharging at several rates. Using the potential measurements, we calculated the current, charging current, and charge stored distribution, which we present here. The results illustrate the transport limitations and provide insight into the level of electrode effectiveness across the thickness.

Analysis Methods

Current.— We have developed an analysis approach for the potential data that uses finite difference methods to numerically estimate the current and volumetric charging current distributions. In addition, by numerically integrating the charging current we can estimate the distribution of the charge stored. The local current density distribution can be determined from the voltage data using Ohm's law, where the differential form is:

$$i = -\sigma \frac{d\phi}{dx} \quad [1]$$

where i is the area-specific current density, σ is the measured electric conductivity, and $d\phi/dx$ is the local potential gradient with x being the through-thickness coordinate. Since we have discretized voltage data, we use second-order accurate finite differencing to linearize the derivative. Additionally, because we can measure local conductivity

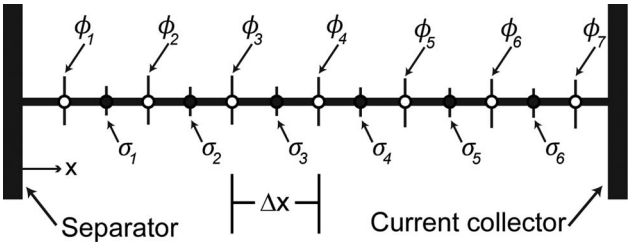

Figure 3. Positions of potential and conductivity measurements in the electrode.

within the electrode, we can implement the finite difference methods using these values rather than an average or global conductivity. However, because the potential measurements and conductivity measurements were taken at different points in the electrode, we have a staggered grid arrangement with discrete conductivity values located between the discrete potential points coinciding with the location of the potential sensing layers. Figure 3 shows a schematic of the staggered grid arrangement for the finite differencing for $M = 7$ sensing layers, and $N = M\text{-}1 = 6$ conductivity measurements.

The finite difference formula for the current with spatially varying conductivity was derived in a similar manner to the typical central difference formula; by averaging first order forward and backward differences for the adjacent discrete points (sensing layer locations) and multiplying each by the corresponding conductivity. In other words, we are averaging the currents estimated from either side of the sensing layer. Eq. 2 shows the modified central difference formula used to estimate the current at the location of an interior sensing layer ($m = 2$ to *M-1*), which maintains second-order accuracy.

$$i_m = [-\sigma_m(\phi_{m+1} - \phi_m) + \sigma_{m-1}(\phi_m - \phi_{m-1})]/2\Delta x + O(\Delta x^2) \quad [2]$$

Here i_m is the local area-specific current density, σ_m is the conductivity, ϕ_m is the measured electric potential, and Δx is the spacing between the sensing layers.

Since a central difference cannot be applied at the first and last sensing layers, Eqs. 3 and 4 are respectively used to calculate the current at these points. To obtain second order accurate differencing, three point forward and backward differences are used to estimate the potential gradient at the end points ($m = 1, M$). To estimate current, we multiply the potential gradient by a second-order accurate forward or backward difference estimate of the conductivity. A complete derivation of the current equations can be found in the supplemental material.[20]

$$i_{m=1} = \frac{-(3\sigma_1 - \sigma_2)}{2}[-3\phi_1 + 4\phi_2 - \phi_3]/2\Delta x + O(\Delta x^2) \quad [3]$$

$$i_{m=M} = \frac{-(3\sigma_{M-1} - \sigma_{M-2})}{2}[\phi_{M-2} - 4\phi_{M-1} + 3\phi_M]/2\Delta x + O(\Delta x^2) \quad [4]$$

Charging current.— To estimate the local volumetric charging current, i_c, we evaluate the second derivative of Ohm's law, sometimes referred to as the current conservation equation. The equation is derived by setting the divergence of the current equal to a local volumetric source or sink of current:

$$i_c = \frac{d}{dx}\left(-\sigma\frac{d\phi}{dx}\right) = \frac{di}{dx} \quad [5]$$

Because we already have local current values, we no longer have to consider the spatial variations of conductivity and the analysis is simplified by allowing us to apply standard finite difference formulas to the current values. Central differencing is applied to the interior points:

$$i_{c,m} = (i_{m+1} - i_{m-1})/2\Delta x + O(\Delta x^2) \quad [6]$$

Three point forward and backward differences are again used at the first and last points as shown in Eqs. 7 and 8.

$$i_{c,m_{fwd}} = (-3i_1 + 4i_2 - i_3)/2\Delta x + O(\Delta x^2) \quad [7]$$

$$i_{c,m_{bkwd}} = (i_{M-2} - 4i_{M-1} + 3i_M)/2\Delta x + O(\Delta x^2) \quad [8]$$

Charge stored.— Additionally, by integrating the volumetric charging current over time we can obtain the amount of charge stored or extracted, Q, over the measurement period.

$$Q = \int_{t_1}^{t_2} i_c dt \quad [9]$$

Eq. 9 is evaluated numerically using the trapezoidal rule approximation:

$$\int_{t_1}^{t_2} i_c dt \approx \frac{(t_2 - t_1)}{2(T-1)} \sum_{k=1}^{T-1} \left(i_{c_{k+1}} + i_{c_k}\right) \quad [10]$$

where T is the number of measurements in time and $t_2 - t_1$ is the total duration of the measurements.

Uncertainty and error propagation analysis.— Error propagation is applied to determine the error associated with the current density, volumetric charging current, and charge stored distributions based on the uncertainty of the parameters used in the finite differencing. Generalized equations for error are shown in Eqs. 11 and 12 for the current density and volumetric charging current data respectively.

$$E_i = \sqrt{\left(E_\sigma \frac{di}{d\sigma}\right)^2 + \left(E_\phi \frac{di}{d\phi}\right)^2 + \left(E_{\Delta x} \frac{di}{d\Delta x}\right)^2} \quad [11]$$

$$E_{i_c} = \sqrt{\left(E_{\Delta x} \frac{di_c}{d\Delta x}\right)^2 + \left(E_i \frac{di_c}{di}\right)^2} \quad [12]$$

In these equations we have used the following uncertainty values: 10 S/m for conductivity, E_σ, 10 μV for potential, E_ϕ, and 20 μm for layer spacing, $E_{\Delta x}$. The value of E_i that was determined in Eq. 11 was used in Eq. 12 to calculate E_{i_c}. The full derivations and final form of the equations used to calculate the error for the forward, backward and central difference current and charging current calculations can be found in the supplemental material.[20]

The error in the estimate of the local charge stored, is determined with a time integration of the charging current error:

$$E_Q = \int_{t_1}^{t_2} E_{i_c} dt \quad [13]$$

When this integration is carried out, the error associated with the initial data increases linearly in time, independent of the charging rate. Thus, over long times when the charging tends to zero, the error dominates over the signal due to the continual integration of constant error.

Experimental

The symmetric aqueous Na^+ EDLC cell was assembled using an acrylic housing for the positive electrode, and an ES comprised of alternating Teflon insulating layers and stainless steel sensing layers for the negative electrode. To make the negative electrode housing, 0.102 mm thick stainless steel sensing layers (TBI, Countryside, IL) were first cut into squares with a long tab protruding from them for electrical connections. Squares of 0.575 mm thick adhesive Teflon (Avrey Dennison, Pasadena, CA) were then adhered to both sides of the sensing layers. The resulting layers were stacked together with double-sided tape (3M, St. Paul, MN, 0.078 mm) in a manner such that each sensing layer tab protruded from the structure in a different direction, allowing easy access to the protruding tabs on each layer.

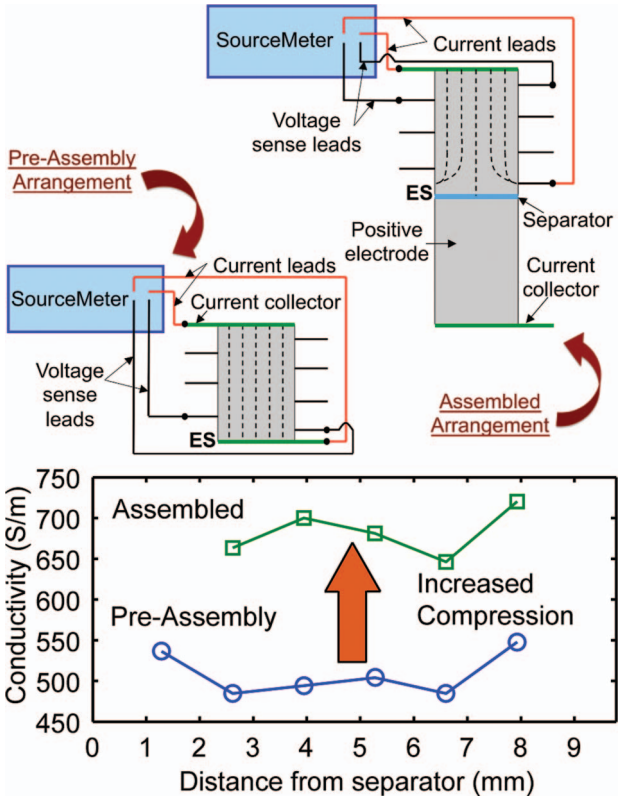

Figure 4. Conductivity through the thickness of the negative electrode using both pre-assembled and assembled configurations of the ES.

The resulting stack thickness of the ES was 9.3 mm. The thickness of the positive electrode housing was similar to the ES at a thickness of 11.2 mm. A 2.38 mm diameter hole was then drilled into the center of both the positive and negative electrode housings. Small holes for alignment pins were also drilled to ensure that the two cylindrical electrodes would align properly after assembly.

The packing of the electrodes into the housings was carried out by alternating between depositing a small amount activated carbon powder (YEC-8 EDLC activated carbon, Fuzhou Yihuan Carbon Co., Fuzhou, China) and injecting 1 M Na_2SO_4(aq) into the holes. A small rod with the same diameter as the holes was then used to tightly pack the activated carbon and electrolyte. This process was continued until the hole was completely filled. A small mound (< 1 mm) was left protruding from each side of both electrode housings to ensure contact between the electrodes, as well as between the electrodes and the current collectors. The mass of the activated carbon needed to fill both the negative and positive electrodes of the capacitor was ca. 0.08 g. The current collectors were secured to the housing using adhesive Kapton (McMaster-Carr, Princeton, NJ).

Before completing assembly with the separator and positive electrode, a resistance distribution measurement was made on the negative electrode using the ES. In the pre-assembly arrangement seen in Figure 4, stainless steel current collectors were placed on both ends of the electrode and connected to a sourcemeter (Keithley 2410 1100V SourceMeter, Cleveland, OH). Another set of Keithley leads were then connected to pairs of sensing tabs and were used to measure the resistance between each tab pair. There are two uses for this measurement in the unassembled arrangement: 1) to compare the conductivity before and after compressing the electrode, 2) to obtain a value for the conductivity between the two sensing layers closest to the separator. The assembled arrangement, also shown in Figure 4, was set up similarly except the sourcemeter was connected to the negative current collector and the sensing tab nearest to the separator. This configuration did not allow for the measurement of the resistance between the two sensing layers closest to the separator, but we estimate this resistance using the value from the pre-assembly configuration and relative change in the resistances between the unassembled and assembled measurements.

After measuring the pre-assembly conductivities, a piece of cotton filter paper separator (Ahlstrom Grade-40, Helsinki, Finland) soaked in 1 M Na_2SO_4 aqueous electrolyte was placed in between the two electrodes. They were then clamped together using 6.35 mm thick stainless steel plates (McMaster-Carr) that were electrically insulated by adhesive Kapton films. Finally, the cell was sealed with epoxy (Loctite, Poxy Pak, Germantown, WI) to prevent solvent evaporation from the separator's perimeter.

Once assembled, the cell terminals were connected to a potentiostat (VSP, Bio-logic, Knoxville, TN) to control the charging and discharging of the cell. Additionally, each of the stainless steel tabs protruding from the sensing layers were connected to the differential voltage measurement inputs on a data acquisition board (DAQ) (National Instruments, Austin, TX) with the voltages being measured with respect to the negative current collector. The input impedance of the differential voltage measurement is specified by manufacturer as >10 GΩ, yielding negligible stray current through the DAQ. Prior to conducting charging and discharging experiments, 5 cycles of cyclic voltammetry (CV) were performed at 0.1 mV/s between 0 V and 0.9 V to condition the cell and to assess the capacitance of the EDLC. Constant voltage charging was then conducted at 0.9 V for four hours, followed by four hours of constant current discharging at 22.5 A/m^2. Additional constant current discharging experiments were conducted at 225 A/m^2, 169 A/m^2 and 112 A/m^2, where each discharge proceeded until the cell voltage dropped to zero. The cell was charged at 0.9 V for four hours before every discharge experiment. Electric potential data from the sensing layers was collected during all of the experiments.

Results and Discussion

Conductivity measurements.— Figure 4 presents the conductivity distributions obtained from resistance measurements before and after assembly. The results show roughly uniform conductivities, however, we see about a 7–10% increase in conductivity at the edges and a roughly 35% increase from the pre-assembly to the assembled configuration. The end point increases are likely due to higher compression at these points because of the protruding mounds of electrode material, and a concentration of the compression at the ends. The overall increase with assembly stems from higher compression of the cell from the end plates when it is fully assembled with a compressible separator that can intrude a small amount into the ES hole. The roughly constant conductivity throughout suggests that there is good carbon connectivity and that there are no voids in the electrode that would significantly affect our electric potential readings during the following studies. We are also able to use these local conductivity values to more accurately calculate the local current, volumetric charging current, and charge stored or discharged. However, as previously stated we were only able to obtain the conductivity between the two tabs next to the separator, σ_1, in the pre-assembly setup. To estimate σ_1 for the fully assembled cell we set the ratio of the overall average conductivity for both cases to the ratio of σ_1 for both cases: $\sigma_{1,assem} = \sigma_{1,\text{pre-}assem}(\sigma_{Avg,assem}/\sigma_{Avg,\text{pre-}assem})$.

Capacitance measurements.— CV and charge/discharge cycles were performed on the EDLC to initially condition the cell for repeatable behavior and characterize the cell by conventional cell-terminal analysis. Figure 5 shows the results of these experiments. The shape of the cyclic voltammogram in Figure 5 indicates a resistive behavior, which is generally observed at scan rates much higher than 0.1 mV/s in more conventional EDLCs.[21] A slow scan rate was required here because of the slow diffusion time-scale, $t_L = L^2/4D_{eff,Na^+}$, expected for the thick electrodes. Assuming a Na^+ diffusivity of 1.33×10^{-5} cm^2/s,[22] and a formation factor (porousity/tortuousity) of 0.1, the

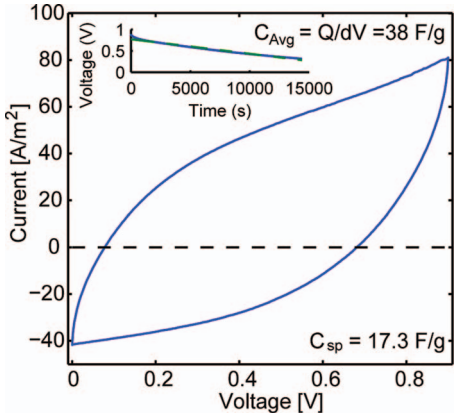

Figure 5. CV conducted at 40 A/m^2 (0.1 mV/s) from 0 V to 0.9 V, yielding a capacitance of 17.3 F/g. The inset shows data for a constant current discharge held at 22.5 A/m^2 for four hours that gives a comparable capacitance result of 38 F/g when taking the slower discharge rate into consideration.

diffusion time-scale for a ∼1 cm thick electrode is around 44 hr. We calculated the full cell's capacitance from the CV data by integrating the area under the forward sweep curve and subtracting the integrated area under the backward sweep curve. Using this method, we calculated a specific capacitance of 17.3 F/g. We verified that the ES and the voltage measurements do not alter the capacitor performance by conducting an additional set of CV measurements with the ES replaced by a piece of acrylic. In those experiments, the standard deviation of the capacitance was 0.67 F/g. The low capacitance value is likely due to the large thickness of the electrode and perhaps incomplete wetting of the activated carbon. It is also interesting to note that the CV appears to have a ∼20 A/m^2 offset, perhaps due to a parasitic reaction current in the cell.

We also experimentally characterized the capacitance from the 22.5 mA/cm^2 constant current discharge experiment (Figure 5 inset) that was conducted after 5 cycles of CV and 4 hours of charging at 0.9 V, using the equation below:

$$Q = \int_{t_1}^{t_2} I/(dV/dt)\,dV, \text{ where } C = Q/dV \qquad [14]$$

where Q is the charge storage capacity, I is the current used to discharge the cell, dV is the total drop in voltage, and dV/dt is the change in voltage over time, which was determined from the slope of the curve, and C is the capacitance of the cell. From Eq. 14, we find the capacitance has a value of 38 F/g, which is roughly double that from the CV data because of the lower currents during this measurements. While the CV was conducted at 0.1 mV/s, corresponding to a discharge current of about 40 A/m^2, the constant current discharge was conducted at only about half that current, 22.5 A/m^2. It is well documented that the capacitance decreases with increasing discharge rates or CV scan rates.[21,23] Additionally, a sharp drop is observed at the start of the discharge data due to the internal resistance.[24] Despite reasonably good agreement between the two methods, the capacitance value is much lower than would be expected for this activated carbon material in thin electrodes.[25]

Potentiostatic charging.— We now discuss the analysis of potentiostatic charging at 0.9 V. This voltage was chosen because it is below that for water electrolysis, which is crucial when using an aqueous electrolyte. Figure 6a shows the raw ES data from a charging cycle conducted immediately after the CV scans were completed. In this plot, the data after 60 s has been smoothed using Gaussian convolution with a standard deviation of 15 s. The first 60 s have not been altered because of the fast transients and order of magnitude higher signal compared to the data after 60 s. Each line in Figure 6a corresponds to a different sensing layer as shown in the bottom left inset. The uppermost line corresponds to the sensing layer closest to the separator,

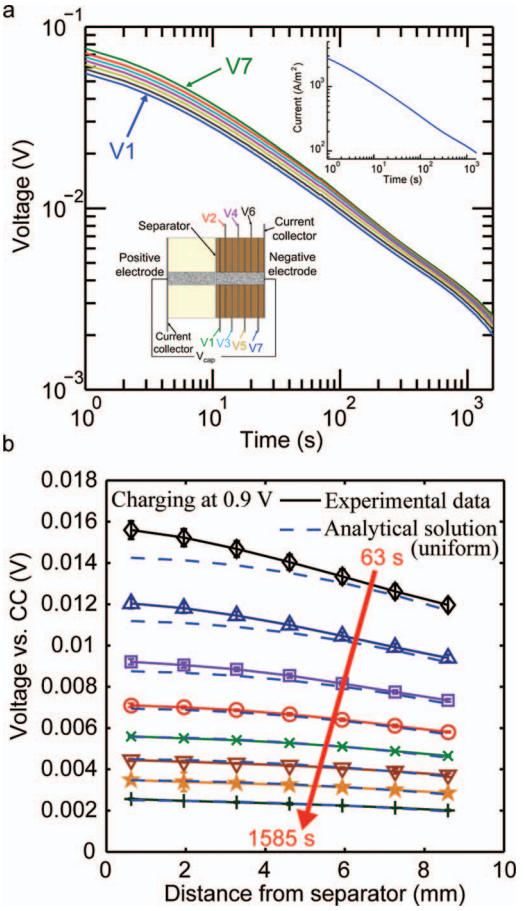

Figure 6. Constant voltage charging at 0.9 V. a. Voltage-time series showing raw potential data from the ES. The top right inset is the corresponding current-time series. The bottom left inset shows the placement of each sensing layer on the ES structure. b. Voltage versus the current collector as a function of the distance away from the separator at eight logarithmically distributed times. The dashed lines are fits to the analytical solution for uniform charging and conductivity. Deviations between the solid experimental data lines and the dashed analytical solution lines indicate non-uniform charging. Symbols denote times plotted: ◊ - 63 s, △ - 100 s, □ - 159 s, ◯ - 251 s, × - 398 s, ∇ - 631 s, ⋆ - 1000 s, + - 1585 s.

while the bottom line is from the sensing layer farthest away. The top right inset shows the corresponding current/time data. Evidence of non-uniform charging can be seen in the raw ES voltage data. At early times, the lines appear to be evenly distributed indicating equal voltage differences, but as the charging proceeds, the lines for the three sensing layers closest to the separator (top three lines) begin to collapse upon each other, while the bottom lines remain evenly spaced apart. Since the electron phase current is proportional to the voltage gradient, the initial uniform spacing indicates the current was constant in regions of the electrode between the sensing layers at early times. This suggests that all of the charging initially occurs between the separator and the first sensing layer as expected. The subsequent closer spacing of the voltages measured near the separator indicates that the current is being consumed by charging in these regions at later times.

These voltage gradients and curvatures can be seen more clearly in Figure 6b. Here, the voltage is plotted versus the distance through the electrode at multiple times. The analytical solution for uniform charging and conductivity is also plotted for comparison.[18] The analytical solution was derived from the conservation of current equation with a fixed potential boundary condition applied at the current collector, $\phi|_{x=L} = \phi_o$, and a zero current boundary condition applied at the

separator, $\partial\phi/\partial x|_{x=0} = 0$, leading to the formula:

$$\phi = \frac{-IL}{2A\sigma_{eff}}\left[\left(\frac{x}{L}\right)^2 - 1\right] + \phi_o \qquad [15]$$

where ϕ is the potential at a given point through the electrode assuming uniform charging and conductivity, I is the cell current, L is the total length, A is the surface area, σ_{eff} is the average effective electric conductivity, x is the distance away from the separator and ϕ_o is the potential at the interface of the electrode with the current collector. Eq. 15 is fitted to the voltage distribution using I as a fitting parameter. All other values are known. It can be seen that at short times the analytical solution for uniform charging and experimental data do not match up well near the separator. In this case, deviance from the analytical solution indicates non-uniform charging. At later times the experiment and model fit curves overlap more, implying that the charging becomes more uniform.

The finite difference equations discussed in the analysis methods section have been used with the voltage data to estimate the local current and volumetric charging current at the location of each sensing layer. The two current estimations are plotted versus the distance away from the separator in Figure 7a and Figure 7b respectively. It can be seen in Figure 7a that at early times the local current is relatively low near the separator and plateaus within a short distance to a maximum value further into the electrode. This shows that the charging is initially concentrated at the separator, since a plateau in the current data indicates a region of zero charging. Two changes are identified in Figure 7a as time proceeds; first, the plateau diminishes and shifts toward the current collector, second, the magnitude of the current decreases in a manner consistent with charging a capacitor at constant voltage. We observe that the current near the separator does not go to zero at long times, but asymptotes to a value of 40–50 A/m^2. This is likely an indicator of a stray current, and is consistent with the current offset in the CV analysis.

We also find a systematic offset in Figure 7a between the current estimate at the final sensing layer and the current measured by the potentiostat at the current collector. We are able to exclude any geometrical effects as we are comparing current densities, which makes them independent of the diameter and area; also inaccuracies in sense layer spacing, within reasonable bounds, does not have a significant effect. One possible explanation that we explored was that this phenomena was a result of the well-documented change in activated carbon conductivity with polarization.[26] However, during our constant current discharge experiments (shown in Figure 8 and the supplement materials[20]) we find that the current always asymptotes to the same value far away from the separator despite the decreasing potential in the cell and using a constant conductivity for our calculations. This suggests that any conductivity change that may be occurring with polarization is negligible. Another possibility is that the cell conditions change during operation due to additional compression and changes in the surface properties. If this were to occur, the resistance values measured prior to testing could be too high, resulting in apparent underestimations of the current. In Figure 7a, we find the relative difference was constant and that a 22% increase in conductivity across the entire electrode would yield local current density values that match those of the current collector. At this juncture, we could have scaled the current according the relative difference to account for the under-estimation of conductivity; however, we chose to present the unaltered data. In future work, we intend to simultaneously or intermittently measure conductivity using AC impedance while the charging or discharging is occurring.

Figure 7b shows an initial peak in the volumetric charging current plot near the separator, which shifts toward the current collector and decreases in magnitude over time. This behavior is consistent with that inferred from the current plot in Figure 7a. At 251 s, the charging current is mostly uniform (red circles); prior to that time the charging current is concentrated in the regions closer to the separator and after that time it is concentrated more toward the current collector. This

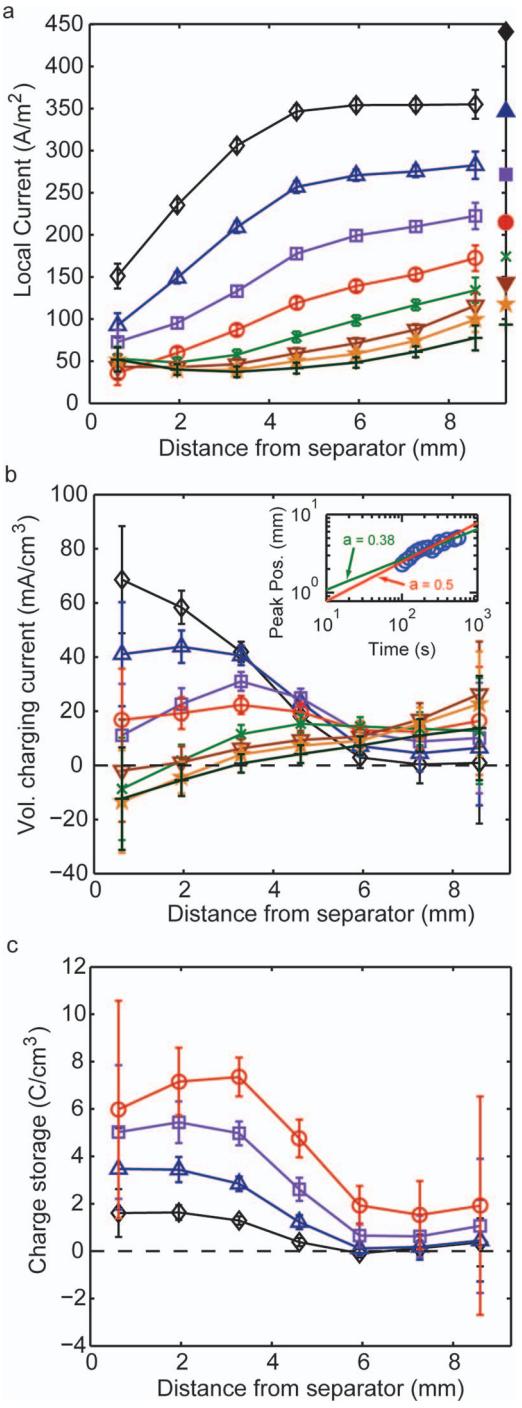

Figure 7. Constant voltage charging at 0.9 V. a. Local current plotted as a function of distance through the electrode. Lower currents near the separator suggest charge storage taking place here. b. Volumetric charging current through the thickness of the electrode. Charging current is high where local current was low. Inset shows the position of the charging current peak through the electrode over time. c. Charge stored through the electrode over time. In all plots: ◊ - 63 s, △ - 100 s, □ - 159 s, ◯ - 251 s, × - 398 s, ∇ - 631 s, ⋆ - 1000 s, + - 1585 s.

is consistent with the excellent match seen between the experimental and analytical voltage distributions from Figure b at 251 s.

In Figure 7b, we observe that negative charging currents are estimated near the separator at long times. Negative currents are unlikely during charging (although they may occur due to a parasitic reaction mechanism) and it is a reasonable conclusion that they arise due to the error in the second derivative estimation. Comparing Figure 7a

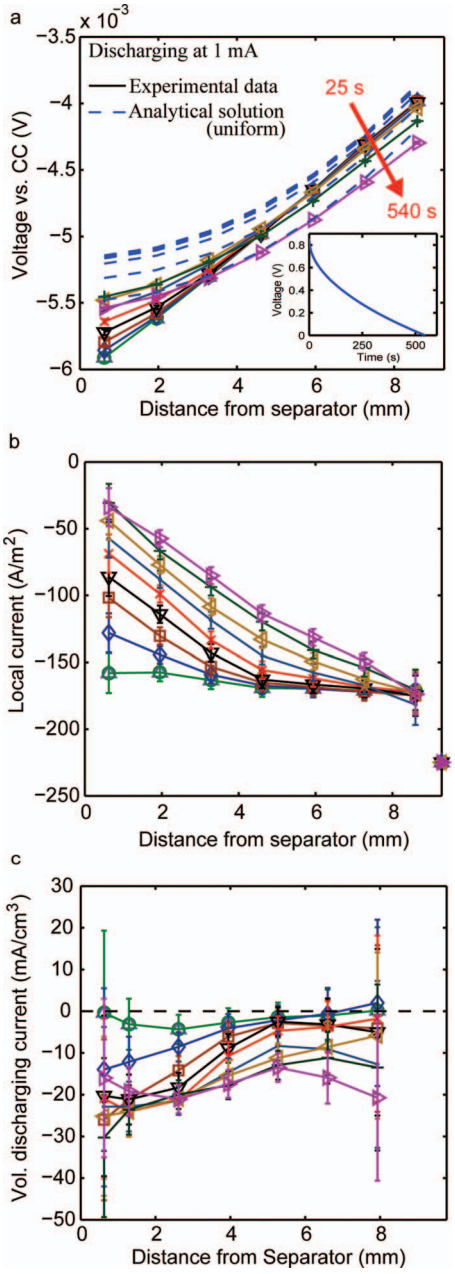

Figure 8. Constant current discharging at 225 A/m^2. a. Voltage versus the current collector as a function of the distance away from the separator and plotted over time. Deviations of the solid experimental data lines from the dashed uniform charging analytical solution lines suggest non-uniform charging in the electrode. b. Local current plotted as a function of distance through the electrode. Higher currents near the separator suggest most discharging taking place here. c. Volumetric discharging current through the thickness of the electrode. Discharging current is high where local current was low. In all plots: △ - 25 s, ◯ - 35 s, ◇ - 50 s, □ - 71 s, ▽ - 100 s, × - 141 s, ● - 200 s, ◁ - 282 s, + - 398 s, ▷ - 537 s.

and 7b, we see increased error estimates with each order of derivative. In addition, there is increased error in estimating the currents at the endpoints, which is a result of the forward and backward differencing formula's functional form.

We can quantify a time-scale for the propagation of charging through the electrode, by analyzing the spatio-temporal charging current data. Here, the time-scale is based on the propagation of the location of the charging current's peak. The inset in Figure 7b shows the location of the peak versus time with logarithmic scaling. The location of the peak is determined by the maximum of a spline fit to the discrete data. The data was fit to a general power law equation, $x_p = bt^{\alpha}$, to extract an estimate of the time-scale parameter, α. A best-fit line to this data gives us a charging time scale of $\alpha \approx 0.38$ with 95% confidence interval bounds of 0.3187 to 0.457. The time-scaling for pure diffusion is $\alpha = 0.5$. In light of the uncertainty, the estimated scaling is indicative of a diffusion process.

Figure 7c shows the results of integrating the volumetric charging current over time to find the amount of charge stored in each section of the electrode. The effects of non-uniform charging are clearly seen here. Although, the amount of stored charge eventually becomes non-zero everywhere, it increases most rapidly and remains highest near the separator. This is consistent with ions needing to diffuse farther through the electrode to reach unoccupied charge sites and having increased transport losses over the longer distances traveled. We can also see from this figure that the charge stored near the separator reaches about 8 C/cm^3, which is much lower than the expected 41 C/cm^3 charge storage capacity we estimated using the Q value determined in Eq. 14. The electrode is not shown to reach full capacity in this figure because only the first 250 s of the data has been plotted. Past this time the error bars become quite large and we lose confidence in the absolute values of our data. In this time frame, however, it is apparent that only about one-third to one-half of the electrode is being used to store charge over this 250 s period. This means that the electrode should be thinner to fully utilize the electrode in this period of time. However, it should be noted that the 5 mm thickness of high electrode effectiveness is two orders of magnitude thicker than state of the art Li-ion batteries; demonstrating the dramatic increases in thicknesses afforded by aqueous electrolytes.

Galvanostatic discharging.— We performed a second set of experiments on analyzing distributions during glavanostatic discharging at current densities of 225 A/m^2, 169 A/m^2, and 112 A/m^2. By discharging galvanostatically we ensure that the current does not decrease over time and therefore our potential distribution's differential does not become too small, giving us a larger signal to noise ratio over the duration of the experiment. Figure 8 shows the potential distribution (a), the local current (b), and the volumetric discharging current (c) in the EDLC during the 225 A/cm^2 discharge. Similarly to the charging data, Figure 8a shows that the measured potential distribution does not match the uniform analytical solution near the separator initially, but becomes more uniform over time.

Figure 8a shows unexpected decreases in the voltages as the discharging progresses. Because the current is being held constant, this decrease must be due to a resistance increase in the cell. It is likely that this resistance is occurring between the final tab and the current collector due to the fact that the curve retains its slope at the current collector, but is offset by a constant amount. One possible explanation would be that passivation is occurring at the current collector during operation causing increased resistance. There were no visual indicators of increased resistance, such as corrosion of the current collector or removal of the electrode material. It should be noted that a change in the resistance at the current collector would not affect the current calculations, as they are only dependent on the change in voltage between the sensing layers, which remains constant.

It is also of interest to note that the parasitic reaction that was seen in the charging data does not appear to occur during discharge. Figure 8b shows that the current at the tab closest to the current collector remains constant over time. We would expect the magnitude of this current to decrease over time, if a parasitic reaction was consuming current within the electrode. The fact that a parasitic reaction is observed during charging, but not during discharge suggests that we can be confident that there is no systematic offset in our REs due to our system and that the discrepancy measured is real. Additional data and a more in depth analysis of this phenomenon can be found in the supplemental material.[20]

To more clearly see the shift in the volumetric discharging current over time, the data in Figure 8c has also been visualized as a spatio-temporal plot in Figure 9. In this figure, the volumetric discharge

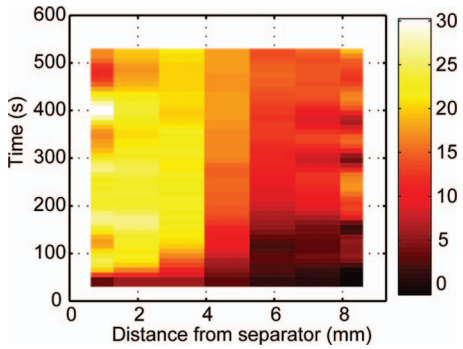

Figure 9. Spatio-temporal plot of the volumetric discharging current. Each color represents the amount of discharging current at a given tab and amount of time through the experiment. The majority of the discharging occurs in the half of the electrode closest to the separator.

current is shown as a function of the distance through the electrode and time. Darker shades represent little to no volumetric discharge current, while lighter shades indicate higher currents. This figure clearly indicates increased volumetric discharging currents in interior sections of the electrode as time goes on, which are difficult to visualize in the line plots of Figure 8c. Additionally, we notice fluctuations in the data that appear to be somewhat correlated across the electrode; i.e., when the current is at a low point of an oscillation the portion of the electrode at the other end exhibits a high point in its oscillation. This is consistent with the constant current discharge where the integral of charging current across the electrode should be constant. Although it is difficult to discern if this is related to noise in the data or the discretization, it could be physical and will be investigated in future work.

In the future, we can improve upon our ES techniques in several ways. First, thinner insulating layers can be used to improve spatial resolution and accuracy of the finite difference discretization. Along these lines, sensing layers will be placed at the separator and current collector separated by a very thin film layer of insulation to obtain data points at the ends of the electrode. Second, the conductivity can be measured during the experiments by performing electrochemical impedance spectroscopy (EIS) in parallel with the DAQ to extract a high frequency resistance. This would alleviate issues with possible differences in conductivity between unpolarized, new electrodes and polarized, conditioned electrodes. Third, we are currently investigating the measurement of the electrolyte potential rather than the electric potential; the key advantage being the larger voltages differences in the electrolyte potential and a higher signal to noise ratio due to the much lower conductivity of the electrolyte.

Conclusions

We have reported on a new technique for measuring in situ, spatio-temporal distributions of electric potential in a porous electrode. Using these potential distributions, we are able to derive spatio-temporal distributions for the current, charging current and amount of charge stored or discharged through the thickness of the electrode. A key objective of this paper was to demonstrate the spatio-temporal measurements possible when using an ES. The potential future uses of this technique are very broad and can be extended to a wide variety of other porous electrode technologies, including fuel cells, Li-ion batteries, redox flow batteries, electrolyzers, etc. The ES can be a valuable tool in assessing distributed phenomena that cannot be determined by other means. For instance, here we were able to demonstrate the high utilization of an ultra-thick activated carbon EDLC electrode using an aqueous Na^+ electrolyte. The results show that the 5 mm of the electrode closest to the separator is well utilized during a four-hour period of charging. This thickness is two orders of magnitude greater than the typical thickness of a Li-ion battery electrode. Furthermore, we have used the ES diagnostics to extract a time-scale for the progression of the charging through electrode as well as identify a potential parasitic mechanism near the separator.

Acknowledgments

The authors acknowledge the support of the National Science Foundation (NSF) through the award of a Facult Early Career Development (CAREER) award for Shawn Litster, as well as support given to Katherine Hess through a Dowd-ICES Fellowship. Additionally, we acknowledge the support of a Pittsburgh Infrastructure Technology Alliance (PITA) grant.

List of Symbols

A	Surface area
C	Capacitance of the cell
$D_{eff,Na+}$	Effective diffusion of Na^+ ions in the electrode
E	Error for a given parameter; subscript denotes parameter
I	Cell current
i	Area-specific current density
i_c	Volumetric charging current density
$i_{c,m}$	Local volumetric charging current density
i_m	Local area-specific current density
L	Total length of the electrode
M	Number of potential measurement points
N	Number of conductivity measurement points
T	The number of measurements in time
t	Time
x	Distance from the separator
Δx	Spacing between sensing layers
Q	Amount of charge stored or extracted

Greek Letters

α	Operation time-scale parameter
σ	Measured electric conductivity
σ_{eff}	Average effective electric conductivity
σ_m	Local electric conductivity
ϕ	Electric potential
ϕ_m	Local electric potential
ϕ_o	Potential at electrode|current collector interface

Subscripts

c	Charging
eff	Effective
m	Finite difference point
o	Point at interface

References

1. R. Kelley and J. S. Vetrano, Basic Needs for Electrical Energy Storage, http://www.sc.doe.gov/bes/reports/files/EES_rpt.pdf, Department of Energy (2007).
2. J. Eyer and G. Corey, Energy Storage for the Electricity Grid: Benefits and Market Potential Assessment Guide, Sandia National Laboratories (2010).
3. Z. Yang, J. Zhang, M. C. W. Kintner-Meyer, X. Lu, D. Choi, J. P. Lemmon, and J. Liu, *Chemical Reviews*, **111**, 3577 (2011).
4. A. D. Tevar and J. F. Whitacre, *Journal of The Electrochemical Society*, **157**, A870 (2010).
5. E. Hittinger, J. F. Whitacre, and J. Apt, *Journal of Power Sources*, **206**, 436 (2012).
6. J. W. Long, D. Bélanger, T. Brousse, W. Sugimoto, M. B. Sassin, and O. Crosnier, *MRS Bulletin*, **36**, 513 (2011).
7. Y.-g. Wang and Y.-y. Xia, *Journal of The Electrochemical Society*, **153**, A450 (2006).
8. J. F. Whitacre, A. Tevar, and S. Sharma, *Electrochemistry Communications*, **12**, 463 (2010).
9. B. Barnett, *Proceedings of the DOE Vehicles Technology Program Annual Merit Review*, Washington, D.C. (2010).
10. K. G. Gallagher, D. Dees, and P. Nelson, in *Proceedings of the DOE Vehicles Technology Program Annual Merit Review*, Washington, D.C. (2011).

11. *CRC Handbook*, CRC Press, Boca Raton, FL (2012).
12. S. J. Harris, A. Timmons, D. R. Baker, and C. Monroe, *Chemical Physics Letters*, **485**, 265 (2010).
13. B. Barnett, in *Proceedings of the DOE Vehicles Technology Program Annual Merit Review*, Arlington, VA (2009).
14. M. Eikerling, A. A. Kornyshev, and E. Lust, *Journal of The Electrochemical Society*, **152**, E24 (2005).
15. J. Liu, M. Kunz, K. Chen, N. Tamura, and T. J. Richardson, *The Journal of Physical Chemistry Letters*, **1**, 2120 (2010).
16. S.-H. Ng, F. La Mantia, and P. Novák, *Angewandte Chemie International Edition*, **48**, 528 (2009).
17. J. B. Siegel, X. Lin, A. G. Stefanopoulou, D. S. Hussey, D. L. Jacobson, and D. Gorsich, *Journal of The Electrochemical Society*, **158**, A523 (2011).
18. K. C. Hess, W. K. Epting, and S. Litster, *Analytical Chemistry*, **83**, 9492 (2011).
19. W. Epting, K. C. Hess, and S. Litster, *ECS Transactions*, **33**, 1241 (2010).
20. See supplementary material at http://dx.doi.org/10.1149/2.028208jes.html TBA.
21. H. Zhou, S. Zhu, M. Hibino, and I. Honma, *Journal of Power Sources*, **122**, 219 (2003).
22. P. Vanysek, in *CRC Handbook of Chemistry and Physics*, D. R. Lide Editor, p. 5, Boca Raton (1993).
23. K. Chan, *Journal of Power Sources*, **142**, 382 (2005).
24. C.-T. Hsieh and H. Teng, *Carbon*, **40**, 667 (2002).
25. Fuzhou Yihuan Carbon Co. Ltd., http://www.yhcarbon.com/index.php?_m=mod_product&_a=view&p_id=188.
26. B. Kastening, M. Hahn, and J. Kremeskötter, *Journal of Electroanalytical Chemistry*, **374**, 159 (1994).